ACS APPLIED MATERIALS & INTERFACES

www.acsami.org

Research Article

Ion Exchange Conversion of Na-Birnessite to Mg-Buserite for Enhanced and Preferential Cu^{2+} Removal via Hybrid Capacitive Deionization

Yang Bao,[†] Jie Jin,[†] Mengyu Ma, Man Li, and Feihu Li*

Cite This: *ACS Appl. Mater. Interfaces* 2022, 14, 46646−46656

Read Online

ACCESS | Metrics & More | Article Recommendations | Supporting Information

ABSTRACT: Layered manganese oxides (LMOs) have recently been demonstrated to be one of the most promising redox-active material platforms for electrochemical removal of heavy metal ions from solution via capacitive deionization (CDI). However, the impact of interlayer spacing of LMOs on the deionization performance of electrodes in a hybrid capacitive deionization (HCDI) system with an LMO cathode and a carbon anode (i.e., LMO/C electrodes), and their phase transformation behaviors, particularly during the desalination operations, have yet to be extensively evaluated. In this study, we thoroughly evaluate Mg-buserite obtained by ion exchange of fresh Na-birnessite and Na- and K-birnessite as HCDI electrodes to remove copper ions (Cu^{2+}) from saline solutions. Among the three LMO/C electrodes, the Mg-buserite/C (MgB/C) electrodes demonstrate the best deionization performance in terms of salt adsorption capacity (SAC), electrosorption rate, and cycling stability, followed by K-birnessite/C (KB/C) and Na-birnessite/C (NaB/C). More importantly, MgB/C exhibits the highest Cu^{2+} ion adsorption capacity (IAC) of 89.3 mg Cu^{2+} per gram electrode materials at a cell voltage of 1.2 V in 500 mg L^{-1} $CuCl_2$ solution, with an IAC retention as high as 96.3% after 60 charge/discharge cycles. Given that electrosorption of Cu^{2+} ions is often competed by alkali and alkaline earth metal ions, our data reveal that the MgB/C electrodes demonstrate selectivities of 4.7, 7.7, and 8.1 for Cu^{2+} over Na^+, Ca^{2+}, and Mg^{2+}, respectively. Moreover, X-ray diffraction and spectroscopic analyses show that the enhanced deionization performance and preference for Cu^{2+} are mainly attributed to the expanded interlayer spacing of LMO minerals. This study provides a promising strategy for tailoring LMO minerals for improving their electrosorption capacity and preference for copper ions from a multivalent-ion solution via an HCDI platform.

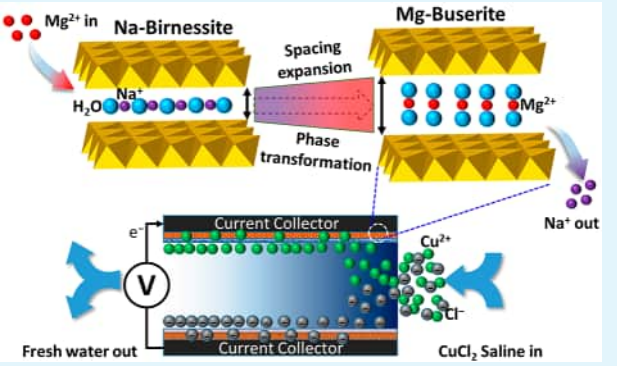

KEYWORDS: *layered manganese oxides, electrochemical desalination, electrosorption, heavy metal, phase transformation, selectivity*

INTRODUCTION

Water scarcity and anthropogenic pollution worldwide have caused a wide variety of global issues relevant to public health, agriculture, industrial production, ecosystems, and the sustainability of our society.[1,2] Heavy metal ions have been commonly found in groundwater and surface waters and categorized as toxic contaminants of public health and environmental concern. Copper ion (Cu^{2+}), in particular, is identified as one of the 14 toxic heavy metals due to its adverse effect on human health, especially when ingested in excess. Primary anthropogenic sources of Cu^{2+} in surface waters include mining, hydrometallurgy, metal plating, printing circuits, fertilizer, and refining industries.[3−6] Conventional approaches to removing aqueous Cu^{2+} ions include ion exchange, adsorption, membrane filtration, and chemical precipitation.[4,7] These processes are often limited and costly due to the need for regeneration with excessive chemicals and extra cost in dealing with the chemical sludge. Therefore, it is crucial to develop innovative methods of sequestering Cu^{2+} at a lower cost, without the use of chemicals or any environmental impacts.

Capacitive deionization (CDI) has been demonstrated as a promising technique for ion separations recently.[8−10] It offers an attractive platform for desalination,[9,11,12] selective ion removal,[13−19] and recovery of high-value elements.[15,16,20,21] Carbon-based materials, e.g., activated carbon, carbon aerogels, carbon nanotubes, graphene, mesoporous carbon, and carbide-derived carbon, are widely used as the electrode materials in CDI.[3,6,22−27] Recent reports have shown that hybridization of the conventional carbon electrodes with Faradaic/redox-active

Received: July 21, 2022
Accepted: October 3, 2022
Published: October 10, 2022

https://doi.org/10.1021/acsami.2c13086
ACS Appl. Mater. Interfaces 2022, 14, 46646−46656

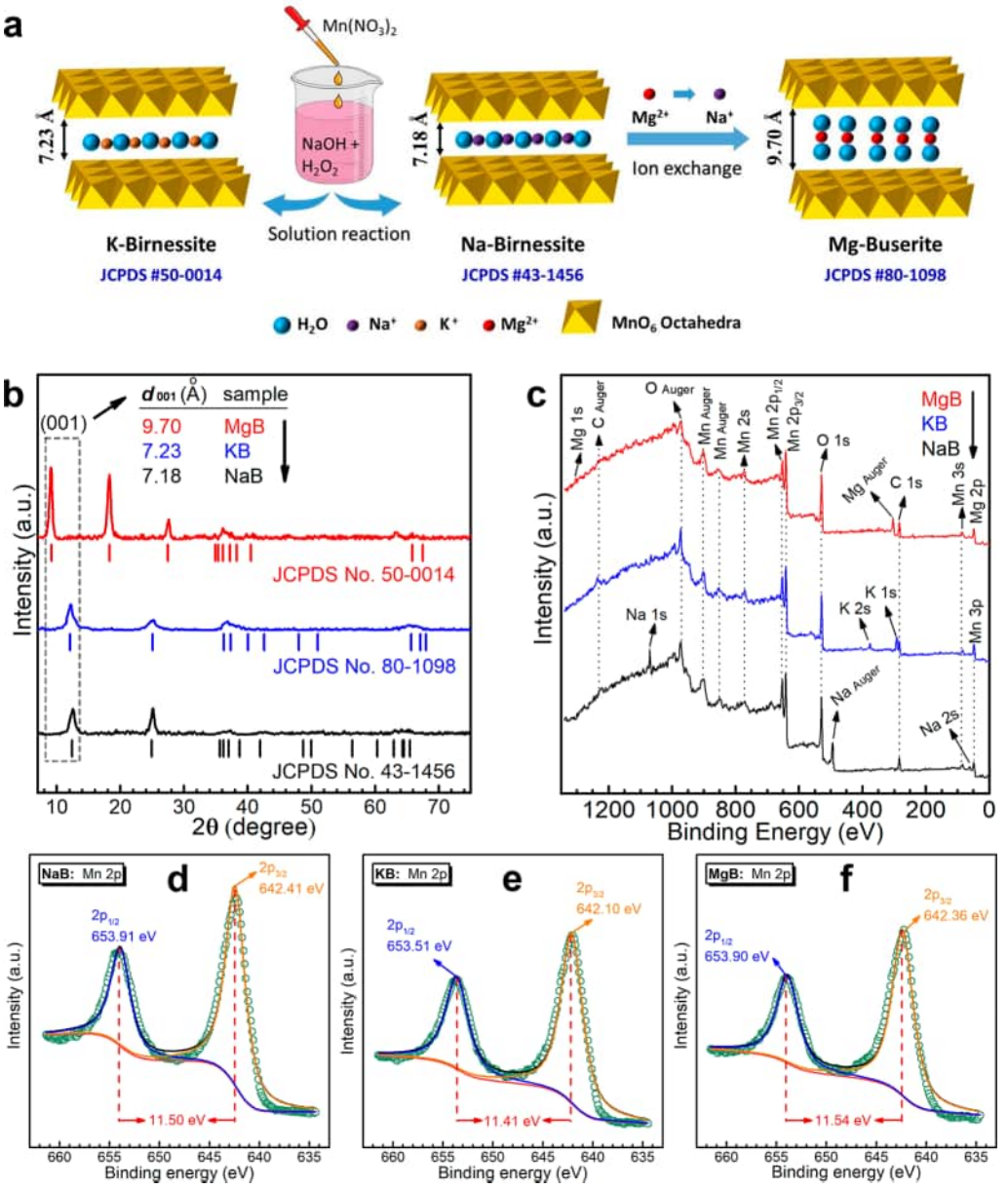

Figure 1. (a) Schematical illustration of the preparation of Na-, K-birnessite (NaB, KB), and Mg-buserite (MgB). (b) XRD patterns. (c) XPS survey spectra. (d–f) Mn 2p XPS regions of NaB, KB, and MgB.

materials can significantly enhance the salt adsorption capacity (SAC) and selectivity for heavy metal ions (e.g., Cu^{2+}, Pb^{2+}, etc.).[4,5,28−32] Redox-active materials can capture and store a significant amount of ions in addition to those electrosorbed by the conventional carbon electrodes. For instance, Liu et al.[28] reported that the electrodeposition of a manganese dioxide (MnO_2) film onto carbon fiber (CF) could significantly improve its SAC for Cu^{2+}. The resultant MnO_2/CF electrodes exhibited a maximum Cu^{2+} adsorption capacity as high as 172.88 mg g^{-1}. Zhang et al.[31] developed redox-active molybdenum dioxide/carbon spheres (MoO_2/C) electrodes to remove Pb^{2+} ions selectively by an asymmetric CDI method. The MoO_2/C electrodes displayed a high Pb^{2+} removal efficiency of >99% in a mixture of 100 mg L^{-1} $Pb(NO_3)_2$ and 100 mg L^{-1} NaCl and high regeneration performance in such mixed solutions. Other compounds, such as zinc sulfide (ZnS),[5] titanium dioxide (TiO_2),[33] and ferriferous oxide (Fe_3O_4),[30] have also been employed as dopants for carbon electrodes used in CDI systems.

Because of their unique properties, including low cost, abundance, environmental benignity, and a high theoretical specific capacitance (i.e., 1370 F g^{-1}), layered manganese oxides (LMOs, i.e., the birnessite–buserite family of layered MnO_2), have gained fast-growing interest over the past decades, especially in CDI systems.[4,29,34−41] Birnessite, in particular, has been extensively studied as a CDI electrode material for electrosorption of Na^+[36−39] and heavy metal ions (e.g., Cu^{2+}, Zn^{2+}, and Ni^{2+})[4,35,42] due to its excellent electrochemical redox activity, large abundance of Mn(IV) vacancies in the MnO_6 octahedra layers, and tailorable surface and interlayer properties. Intentionally expanding the interlayer spacing in layered materials has been well-established as a successful strategy to improve their performance in ion sieving,[43] electrochemical energy storage,[44,45] and Na^+ storage.[46] Recent works have demonstrated enhanced ion

https://doi.org/10.1021/acsami.2c13086
ACS Appl. Mater. Interfaces 2022, 14, 46646−46656

adsorption capacities for Na^+ ions by increasing the interlayer spacing of birnessite via ion exchange of sodium ions (Na^+) with magnesium ions (Mg^{2+}).[36,37] Ion exchange treatment of the pristine Na-birnessite (NaB) in a magnesium chloride ($MgCl_2$) solution led to a phase transformation from NaB to Mg-buserite (MgB), with the interlayer spacing increasing from 7.2 to 9.7 Å and the SAC growing from 31.5 to 37.2 mg g^{-1}.[37] Nevertheless, the electrochemical interaction of MgB with heavy metal ions (e.g., Cu^{2+}) in a CDI platform has not been systematically explored.

In this study, we investigate the electrosorption performance of three LMO-based electrodes for Cu^{2+} ions in an HCDI system using carbon as an anode and LMO as a cathode (i.e., LMO/C electrodes) and evaluate the preference of MgB/C electrodes for Cu^{2+} over alkali and alkaline earth metal ions. Insights into the enhanced electrosorption of Cu^{2+} are systematically elucidated through structural characterization, electrochemical analysis, and CDI desalination experiments. The effects of cell voltage and salt concentration of the feed solution on the desalination performance are examined, as well as the cycling stability of the LMO/C electrodes. In addition, the mechanisms of Cu^{2+} uptake are elaborated by X-ray diffraction and photoelectron spectroscopic analyses.

EXPERIMENTAL SECTION

All chemicals used in this study were of reagent grade quality or above and purchased from Sinopharm Chemical Reagent Co., Ltd. (Shanghai, China) unless otherwise specified. All solutions were prepared using deionized water (DI H_2O, resistivity ≥ 18 MΩ·cm at 25 °C).

Preparation and Characterization of Birnessite/Buserite Materials. Na-birnessite (NaB) was prepared using a modified solution reaction/precipitation method (Figure 1a, Text S1).[47] By replacing sodium hydroxide (NaOH) with potassium hydroxide (KOH), K-birnessite (KB) was synthesized following the same procedure. Mg-buserite (MgB) was synthesized via an ion exchange approach (Figure 1a).[37] More experiment details and structural characterization are presented in Texts S1 and S2.

Electrochemical Measurements. Electrochemical measurements, including cyclic voltammetry (CV), galvanostatic charge−discharge (GCD), and electrochemical impedance spectroscopy (EIS), were performed on a CS310H electrochemical workstation (Correst, Wuhan, China). These tests were carried out in a 1.0 M NaCl solution with a three-electrode system. The three-electrode configuration consists of a working electrode (1 × 1 cm^2), a platinum (Pt) foil counter electrode (1 × 1 cm^2), and an Ag/AgCl (3.0 M KCl) electrode (reference electrode). The details of all electrochemical characterization are given in Text S3.

Desalination Experiments. We determined the desalination performance of the LMO minerals on a homemade HCDI device (Figure S1). Graphite papers were used as anodes, and cathodes were prepared by coating a mixture of LMOs (~0.05 g), acetylene black, and PVDF with a mass ratio of 8:1:1 onto the graphite paper (10 × 10 cm^2) on a platen heater at 60 °C followed by heating in a vacuum oven at 80 °C for 12 h. The obtained cathodes have an active desalination area of 5 × 5 cm^2 and an average thickness of ~0.1 mm. The detailed procedures for CDI electrode fabrication can be found elsewhere.[39] A batch-mode operation was used to run the HCDI cell with a volume of 5 mL. A total volume of 40 mL of saline solution (50−1000 mg L^{-1}, ppm) was continuously circulated through a peristaltic pump (BT-100, Longer Precision Pump Co., China) at a flow rate of 40 mL min^{-1}. To determine the selectivity (defined as the ratio of the percent of Cu^{2+} removed to the percent of other competing ions removed, also known as a separation factor)[48] of the electrode toward Cu^{2+} over other monovalent and divalent ions (i.e., Na^+, K^+, Mg^{2+}, and Ca^{2+}), saline water was sampled at intervals of 5 charge/discharge cycles and analyzed with an Optima 8000 Inductively Coupled Plasma-Optical Emission Spectrometry (ICP-OES) apparatus (PerkinElmer Inc., USA). More details of the desalination operation are presented (Text S4).

RESULTS AND DISCUSSION

Physicochemical Characteristics of As-Prepared LMOs. Birnessite is a ubiquitous oxide mineral of manganese-(III, V) in various natural environments. The naturally occurring birnessite generally contains foreign ions (i.e., Na^+, K^+, and Ca^{2+}) as stabilizing cations in the interlayer region.[49] To elucidate the effects of stabilizing cations on the interlayer spacing of LMOs and thus their ion storage performance, we prepared three types of LMOs stabilized respectively by Na^+, K^+, and Mg^{2+} ions (Figure 1a). The as-prepared LMO minerals include Na-birnessite, K-birnessite, and Mg-buserite, abbreviated as NaB, KB, and MgB. Crystallographic analyses indicated that the X-ray diffraction (XRD) patterns of the as-prepared NaB, KB, and MgB match well with the standard XRD patterns of Powder Diffraction File nos. 43−1456, 80−1098, and 50−0014, respectively (Joint Committee on Powder Diffraction Standards, Figure 1b). In addition, MgB, KB, and NaB show interlayer spacing (d_{001}) of 9.70, 7.23, and 7.18 Å, with grain sizes of 13.5, 7.8, and 30.7 nm, respectively, which are in good agreement with the data reported elsewhere.[37,49] Note that Mg, K, and Na are respectively detected on the X-ray photoelectron spectroscopy (XPS) spectra (Figure 1c), implying that these elements appear to play as the stabilizing ions for MgB, KB, and NaB, respectively. The two spin−orbit peaks in Mn 2p XPS regions assignable to Mn $2p_{1/2}$, and Mn $2p_{3/2}$ exhibited spin−orbit splitting values (ΔE) of 11.50, 11.41, and 11.50 eV for MgB, KB, and NaB, respectively (Figure 1d−f). Furthermore, the Mn 3s XPS region showed spin−orbit peak splitting with ΔE of 4.80, 4.86, and 4.97 eV (Figure S2b,d,f), indicative of an oxidation state of Mn^{4+} in these samples.[29,39,50] The O 1s region (Figure S2a,c,e) can be differentiated as the tetravalent oxide (Mn−O−Mn), the hydrated trivalent oxide (Mn−O−H), and the residual water molecular (H−O−H).[39] This finding is in agreement with the FTIR spectra (Figure S3a), which demonstrated the surface oxygen species are attributed to surface hydroxyl groups (~3415 cm^{-1}), water vapor (~1617 cm^{-1}), and metal oxide (400−600 cm^{-1}).[51] Moreover, the X-ray fluorescence spectroscopy (XRF) spectra confirm the material compositions of these LMO minerals as evidenced by the principal K-shell emission lines assignable to Mg, K, Na, and Mn (Figure S3b), in good consistence with the above XPS results and the findings reported previously.[37]

SEM images show that these materials are featured by irregular aggregates (Figure S4a−c). In contrast, the hydrothermal treated Na-birnessite exhibits a plate-like morphology stacked together (Figure S4d). Pore structure results (Figure S5 and Table S1) indicate that all these samples exhibit type IV isotherms with hysteresis loops of type H2 at high relative pressure ($P/P_0 > 0.4$) according to the International Union of Pure and Applied Chemistry (IUPAC) classification, implying that all these samples have well-defined mesopores. These results are further confirmed by the BJH pore size distribution (PSD) plots (Figure S5b,d), in which NaB and KB exhibited a narrow PSD centered at mean pore sizes of ~23.3 and 12.6 nm, respectively, whereas MgB showed a broad PSD with two mean pore sizes of ~26.4 and 39.2 nm, respectively. The specific surface areas (S_{BET}) are ~75, 137, and 73 m^2 g^{-1} for MgB, KB, and NaB, respectively (Table S1), which are in

https://doi.org/10.1021/acsami.2c13086
ACS Appl. Mater. Interfaces 2022, 14, 46646−46656

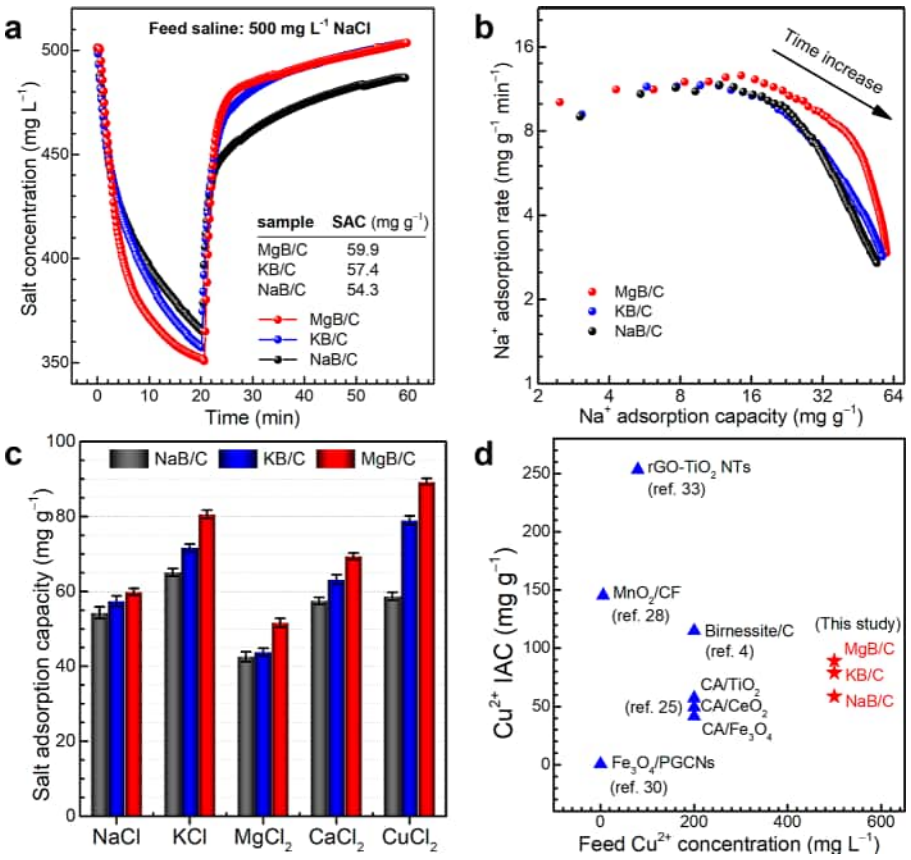

Figure 2. (a) Plots of salt concentration versus time in the third run of HCDI operation with the LMO/C electrodes in a 500 mg L^{-1} NaCl saline. (b) The corresponding Kim−Yoon plots. (c) SACs of the LMO/C electrodes in 500 mg L^{-1} saline with different salts. (d) Comparison of Cu^{2+} IACs of metal oxide based electrodes applied for CDI.

reasonable accordance with the particle size distribution data and are also comparable to those reported elsewhere.[4,52]

Electrochemical Performance. CV profiles of the LMO/C (i.e., MgB/C, KB/C, and NaB/C) electrodes in a 1 M NaCl solution, as shown in Figure S6, demonstrated leaflike-shaped voltammograms at high scanning rates (i.e., 50 and 100 mV s^{-1}). This phenomenon indicates a less-than-ideal capacitive behavior, especially when compared to carbon-based electrodes.[38,39] These CV curves are distorted with redox peaks over the potential window of 0−0.8 V (Figure S6d), which is likely due to the Faradaic reactions of the redox-active MnO_2. This finding further confirms the reversible redox activity of these electrodes.[53] In addition, the MgB/C electrodes demonstrate the largest integrated area under the CV curve, implying that it has the maximal specific capacitance and probably the best desalination performance among these electrodes.

As shown in Figure S7, all GCD curves are featured by a set of well-defined and nearly symmetric triangles, suggesting that these LMO/C electrodes have high reversibility of redox activity during the charge and discharge operations with negligible IR drop in the discharge processes (Figure S7e).[54] The specific capacitances calculated from the discharge profiles after the IR drop show a negative correlation with the specific current as expected (Table S1) and decrease apparently in the order of MgB/C > KB/C > Na/C (Figure S8a). For instance, the specific capacitance of MgB/C is as high as 276.9 F g^{-1} at 0.3 A g^{-1} vs those of NaB/C and KB/C (i.e., 203.0 and 213.5 F g^{-1}, respectively). The electrochemical impedance spectroscopy (EIS) profiles (Figure S8b) suggest that MgB/C has a charge-transfer resistance (R_{ct}) as minor as 1.4 Ω (cf. 2.21 and 1.84 Ω for NaB/C and KB/C, respectively), indicating the highest charge transfer rate at the interface of MgB/C and the electrolyte. In addition, the sloped portion in the intermediate- and low-frequency regions known as the Warburg resistance is the consequence of the frequency dependency of ion transport from the electrolyte to the electrode.[55] A higher slope in the profile implies a greater Warburg resistance. Note that the slopes in the range of 10−25 Ω decrease in the order NaB/C > KB/C > MgB/C (Figure S8b), suggesting that the MgB/C electrode has the highest interfacial ion migration rate among these electrodes.[39,56]

Capacitive Deionization Performance. The deionization performance of these LMO/C electrodes was evaluated based on batch-mode HCDI experiments in saline waters with various ions (i.e., Na^+, K^+, Mg^{2+}, Ca^{2+}, and Cu^{2+}). When a cell voltage of 0 V was applied between the graphite paper anode and the NaB cathode in the HCDI cell containing 100 mg L^{-1} (573.8 μmol L^{-1}) Cu^{2+} ions, no changes in the Cu^{2+} concentration were observed (Figure S9), implying no static adsorption occurred. This phenomenon is mainly due to ion exchange membranes in the HCDI cell, preventing ions from transporting across the membrane into the electrode regions without a driving force (e.g., a cell voltage).[57] However, when a cell voltage of 1.2 V was applied, Cu^{2+} ions passed through the membrane rapidly. Then, they were captured by the cathodes, leading to a drop of Cu^{2+} concentration by 28% in ∼500 s (Figure S9). Notably, the NaB/C electrodes can be efficiently

https://doi.org/10.1021/acsami.2c13086
ACS Appl. Mater. Interfaces 2022, 14, 46646−46656

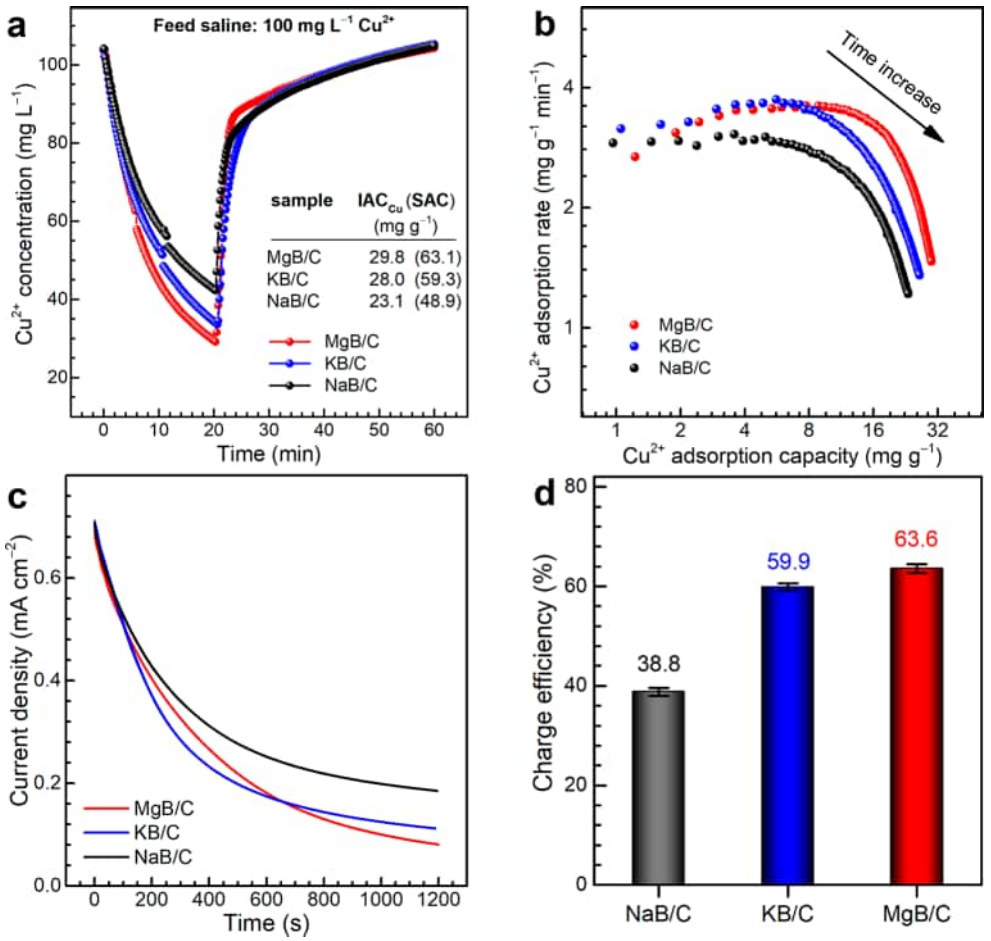

Figure 3. (a) Plots of Cu^{2+} concentration versus time in the third run of HCDI with the LMO/C electrodes in a 100 mg L^{-1} Cu^{2+} saline. (b) The corresponding Kim−Yoon plots. (c) Plots of the response current density versus time during the desalination operation. (d) The charge efficiency of the LMO/C during the charging process in a 100 mg L^{-1} Cu^{2+} saline.

regenerated upon reversing the cell voltage for 160 s, implying fast desorption kinetics.

The LMO/C electrodes were first tested at 1.2 V in the HCDI cell containing 500 mg L^{-1} of NaCl as the saline water. As shown in Figure 2a, the MgB/C electrodes demonstrated a more rapid decrease in the salt concentration than other LMO/C electrodes, implying a much faster Na^+ adsorption rate of MgB/C compared to other electrodes (Figure 2b). Moreover, MgB/C demonstrated the largest adsorption capacity (59.9 mg g^{-1}) than other electrodes (i.e., NaB/C and KB/C) under the same circumstances (Figure 2a), which could be attributed to the maxima interlayer spacing in MgB (see Figure 1a,b), allowing for much more amount of Na^+ ions to be intercalated and stored.[37] Note that both the Na^+ adsorption capacity and the Na^+ adsorption rate of these LMO/C electrodes are positively correlated to the interlayer spacing of the pristine LMOs (Figures 1b and 2b), in good agreement with previous reports.[31,32] In addition, all the LMO/C electrodes demonstrated higher SACs for Na^+, which vastly outstrip most of the manganese oxide/carbon-based electrodes applied for CDI (Table S2). This finding could be ascribed in part to the ion-exchange membranes, which enhanced the charge storage performance of HCDI cells and thereby improved their deionization performance compared to CDI.[57]

Extended applications of these LMO/C electrodes for capacitive removal of other metal ions (e.g., K^+, Mg^{2+}, Ca^{2+}, and Cu^{2+} ions) revealed that their deionization performance followed the same trends as observed above for Na^+ ions, with the orders of both the SACs and the salt/ion adsorption rates of MgB/C > KB/C > NaB/C (Figures 2 and S10−S13, and Tables S2 and S3). To compare the actual deionization performance of the LMO/C electrodes in different saline solutions, we used the normalized salt adsorption capacity (refers to SAC normalized to the molar weight of the salt removed, in μmol g^{-1}) rather than the conventional salt adsorption capacity (in mg g^{-1}). As given in Table S3, all LMO/C electrodes demonstrated a greater normalized SAC in saline water containing alkaline metal ions (i.e., Na^+ and K^+) than in solutions with alkaline earth and heavy metal ions (i.e., Mg^{2+}, Ca^{2+}, and Cu^{2+}). This observation is probably because the singly charged Na^+ or K^+ ions with smaller hydrated radii diffused more facilely in the interlayer region of LMOs than the doubly charged ions with larger hydrated radii (i.e., Mg^{2+}, Ca^{2+}, and Cu^{2+}).[37,58]

Note that the SACs (in μmol g^{-1}) of MgB/C for all metal ions studied, vs those of NaB/C electrodes, have been greatly enhanced after expanding the interlayer spacing of the pristine NaB via ion exchange and thereby being transformed to MgB (Table S3). The enhancement values for Na^+, K^+, Mg^{2+}, and Ca^{2+} were 10.3, 23.8, 21.1, and 20.7%, respectively.

https://doi.org/10.1021/acsami.2c13086
ACS Appl. Mater. Interfaces 2022, 14, 46646−46656

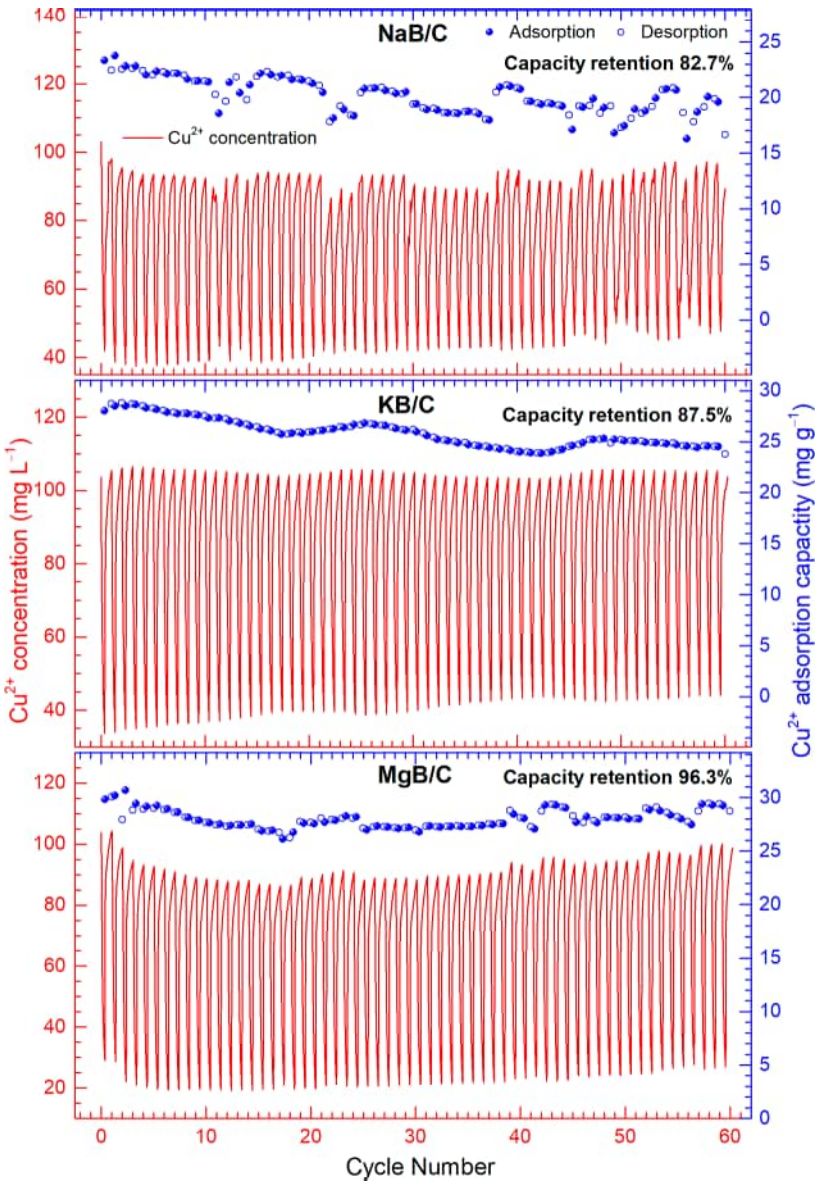

Figure 4. Cycling stability and the Cu^{2+} adsorption−desorption capacity of NaB/C, KB/C, and MgB/C electrodes in a 100 mg L^{-1} of Cu^{2+} solution at a cell voltage of 1.2/−1.2 V.

Interestingly, the maxima SAC (in μmol g^{-1}) of MgB/C for Cu^{2+} in a 500 mg L^{-1} of $CuCl_2$ solution has been improved by 52.1% compared to NaB/C. This finding indicates a higher affinity of Mg-buserite for Cu^{2+} than for alkaline and alkaline earth metal ions.[59] Moreover, IACs of these LMO/C electrodes in a 500 mg L^{-1} of $CuCl_2$ solution are comparable to other CDI electrodes reported in the literature (Figure 2d and Table S4), demonstrating the promise of our electrochemical platform with the LMO/C electrodes for the efficient removal of Cu^{2+} ions from wastewater.

Effect of Cell Voltage and Feed Saline on Removal of Cu^{2+}. To optimize the deionization performance for Cu^{2+} ions, we further evaluate the LMO/C electrodes over a set of cell voltages in saline water of $CuCl_2$ ranging from 50 to 1000 mg L^{-1} (371.9−7437.7 μmol L^{-1}). Considering that Cu^{2+} ion is often the target ion of concern due to its more significant environmental impact and health risk than Cl^- ion, Cu^{2+} ion adsorption capacity (IAC_{Cu}) rather than SACs was an essential indicator of deionization performance.[4,6,14] Note that the IACs of these LMO/C electrodes were positively correlated to the cell voltage applied in HCDI (Figure S14), in good consistent with other previous reports.[60,61] Interestingly, the IACs exhibited a confused dependence on the initial salt concentration (C_0) of the $CuCl_2$ saline solution ranging from 50 to 1000 mg L^{-1} (Figure S14a−c) but demonstrated a clear positive correlation with C_0 in the range of 50−200 mg L^{-1} (Figure S14d). This phenomenon is likely due to the side reactions (e.g., catholic O_2 reduction)[59,61] during the HCDI operation at higher cell voltages (e.g., > 1.2 V). To verify this speculation, we monitored the *in situ* changes in solution pH during the desalination operation over the MgB/C electrodes in a 1000 mg L^{-1} of $CuCl_2$ solution and presented the data in Figure S15. The desalination operation at cell voltages of 0.8−1.2 V has led to a change in solution pH of less than 1 unit, demonstrating a stable desalination behavior of the MgB/C electrodes. An increase in the cell voltage up to 1.4 V, as shown in Figure S15, has resulted in a drop in solution pH from 4.7 to 3.2. This is attributed to the side reaction of O_2 cathodic

https://doi.org/10.1021/acsami.2c13086
ACS Appl. Mater. Interfaces 2022, 14, 46646−46656

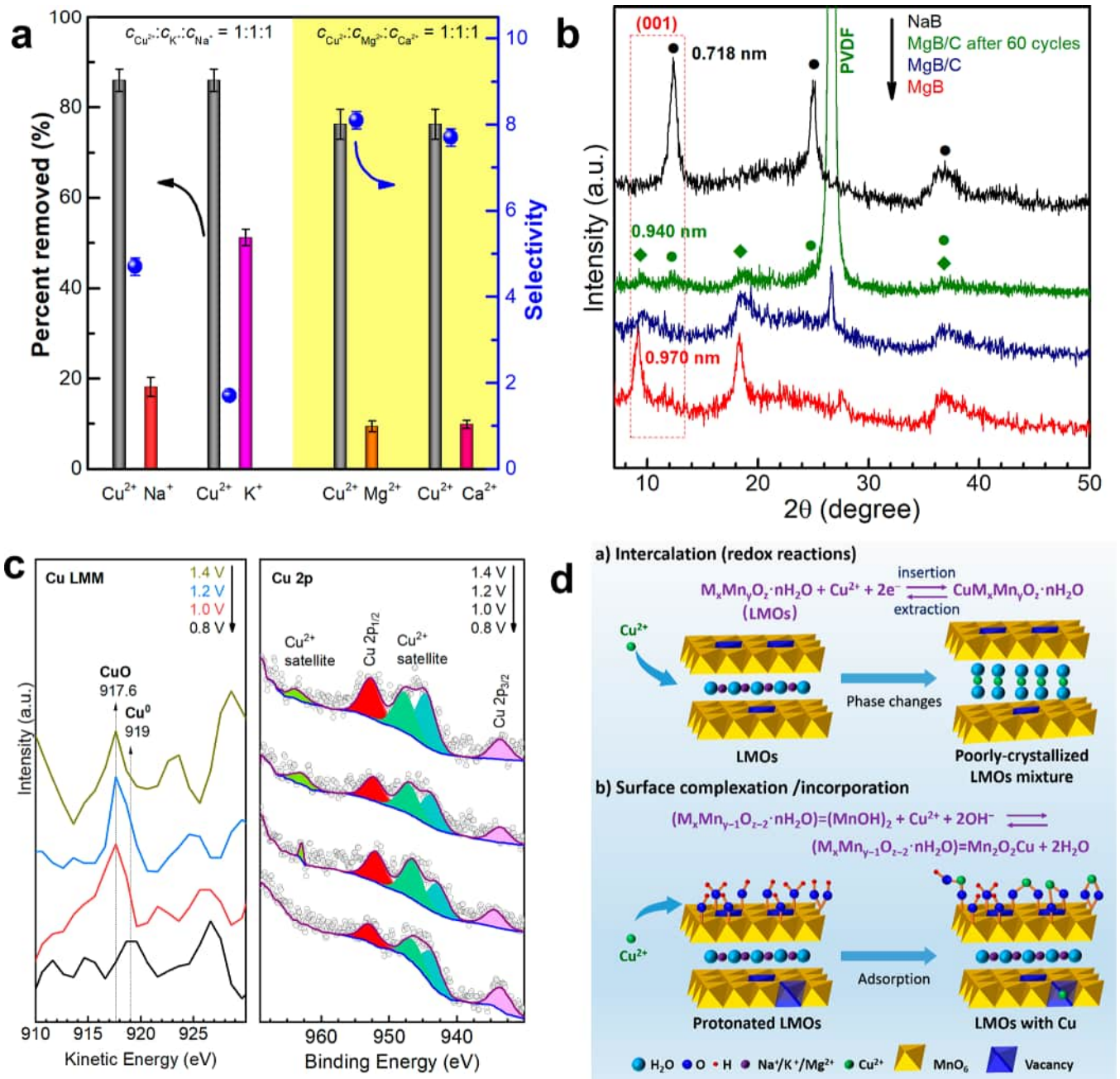

Figure 5. (a) Percent removed, and selectivity of MgB/C electrodes in feed saline containing 0.3 mM Cu^{2+}, 0.3 mM K^+, and 0.3 mM Na^+ (1:1:1 $Cu^{2+}/K^+/Na^+$), and 0.3 mM Cu^{2+}, 0.3 mM Mg^{2+} and 0.3 mM Ca^{2+} (1:1:1 $Cu^{2+}/Mg^{2+}/Ca^{2+}$). (b) XRD patterns of MgB/C electrodes before and after 60 charge/discharge cycles in a 100 mg L^{-1} of Cu^{2+} solution at 1.2/−1.2 V. ●, reflections of Na/Cu-birnessite; ◆, reflections of Mg/Cu-buserite. (c) Cu LMM and 2p XPS regions of MgB/C electrodes after 60 charge/discharge cycles at 0.8−1.2 V. (d) Schematic illustration of Cu^{2+} removal from saline via both the intercalation (redox reactions) and the surface adsorption mechanisms.

reduction occurring at the surface of the carbon constituent in the MgB cathode.[60,62] Minimal pH change in the solution during the CDI operation is beneficial for the long-term operation and thus the overall desalination performance of the electrodes.[51] To this end, a cell voltage of 1.2 V was adopted as the optimal working voltage (Figure S16), just as it has been widely used by the CDI community (Tables S2 and S4). Figure 3 presents the desalination results of these LMO/C electrodes at 1.2 V in a 100 mg L^{-1} Cu^{2+} solution. The MgB/C electrodes demonstrated the best deionization performance for Cu^{2+} ions in terms of ion adsorption capacity, rate, and charge efficiency, followed by KB/C and NaB/C, which is consistent with the above cases of 500 mg L^{-1} saline water with different ions (Figures 2 and S10−13). When assuming no energy was recovered during discharge, our HCDI cell with the MgB/C electrodes demonstrates a pretty low volumetric energy consumption (E_V) of 2.96 Wh m^{-3}, with specific energy consumption (E_{Cu}) of 0.079 Wh g^{-1} for Cu^{2+} ions, showing a good potential application in electrochemical remediation of waste streams polluted by copper ions.

We also studied the cycling stability of the electrodes at 1.2/−1.2 V in a 100 mg L^{-1} Cu^{2+} solution and plotted the data in Figure 4. All electrodes exhibit high reversibility of the adsorption−desorption process for 60 charge/discharge cycles.

https://doi.org/10.1021/acsami.2c13086
ACS Appl. Mater. Interfaces 2022, 14, 46646−46656

The MgB/C electrodes demonstrate superior cycling stability, followed by KB/C and NaB/C electrodes in terms of IAC retention (Figure 4 and Table S5). For instance, the NaB/C electrodes show slightly inferior cycling stability vs both the MgB/C and KB/C electrodes, with an IAC fluctuating within the range of 16.3−23.7 mg g^{-1} (Figure 4) and an IAC recession of 17.3% after 60 charge/discharge cycles (Table S5). The loss in IAC is most likely caused by the increased disorder in the lamellar stacking of MnO_6 octahedra layers of the NaB/C electrodes, as observed previously.[36,39] Besides, the oxidation of the carbon constituent in the cathode (NaB/C) would also contribute in part to the decay of Cu^{2+} ion adsorption capacity.[39,63] In contrast, the MgB/C electrodes, after 60 consecutive intercalation-deintercalation of Cu^{2+} cycles, demonstrate an IAC retention as high as 96.3% (Table S5), despite a minor fluctuation in IACs, was observed during the Cu^{2+} ion adsorption/release cycles (Figure 4).

The preference of MgB/C electrodes toward Cu^{2+} over other monovalent (i.e., Na^+ and K^+) and divalent ions (i.e., Ca^{2+} and Mg^{2+}) from a saline solution containing such ions of concern were also tested after 20 cycles. The results are shown in Figure 5a, which depicts both the percent removed of different ion couples (e.g., Cu^{2+} vs Na^+) and the corresponding selectivity as a function of the ion couples. In the case of feed saline with 1:1:1 $Cu^{2+}/K^+/Na^+$, the average percent removed of Cu^{2+} is as high as 86.0%, whereas the percentages of K^+ and Na^+ are 51.2 and 18.2% respectively, yielding average selectivity values of ∼1.7 and 4.7 for Cu^{2+} over K^+ and Na^+. This finding implies a preference of MgB/C electrodes toward divalent Cu^{2+} over monovalent Na^+ and K^+. This selectivity is comparable to other intercalation electrodes such as vanadium hexacyanoferrate (VHCF) which also demonstrated a separation factor of 3.5 for Ca^{2+} over Na^+ in an HCDI platform.[64] A high selectivity of 18.0 for Ca^{2+} over K^+ was also reported in an HCDI setup using an electrochemically activated layered MnO_2 cathode.[65] Interestingly, the percent of Cu^{2+} removed dropped moderately from 86.0 to 76.3% when substituting the 1:1:1 $Cu^{2+}/K^+/Na^+$ feed saline with an equimolar ternary solution of divalent ions (i.e., $Cu^{2+}/Mg^{2+}/Ca^{2+}$ = 1:1:1). This may be due in part to a blockage of diffusion and mass transfer of Cu^{2+} ions into the LMO interlayers by these divalent ions (i.e., Mg^{2+} and Ca^{2+}) with larger hydrated radii. Nevertheless, higher selectivity values of ∼8.1 and 7.7 for Cu^{2+} over Mg^{2+} and Ca^{2+} were obtained for the feed saline of divalent ions, suggesting a much stronger preference of MgB/C electrodes toward Cu^{2+} over divalent Mg^{2+} and Ca^{2+}. This electrode-intrinsic selectivity of Cu^{2+} appears to be attributed to the higher affinity of LMOs toward Cu^{2+}, which will be further elucidated in the following section.

Mechanisms for Copper Ions Sequestration. To understand the mechanism of Cu^{2+} removal on these LMO/C electrodes, we explored the structural and compositional changes of the electrodes before and after the cycling tests by XRD and XPS characterizations, respectively. It is worth noting that a new peak at $2\theta = 26.7°$ assignable to the (021) reflection of the PVDF binder appeared in the profiles of all electrodes as expected and that mixing with PVDF binder and amorphous carbon black for the preparation of the electrode depressed the peak intensity of LMOs somewhat (Figures 5b and S17). A similar phenomenon was also reported elsewhere.[66] It is clear that after cycling in a 100 mg L^{-1} Cu^{2+} solution for 60 cycles, the XRD pattern of NaB/C changed significantly compared to that of the pristine electrodes (Figure S17a). The emerging peaks labeled with diamonds could be indexed to the reflections of Cu-buserite.[67] Additionally, d_{001} spacing of NaB decreased slightly from 7.18 to 7.10 Å due to ion exchange of Na^+ with Cu^{2+}, leading to a transformation of a fraction of Na-birnessite into Cu-birnessite.[68] These observations demonstrate that when the NaB/C electrodes were cycled in a 100 mg L^{-1} Cu^{2+} saline Cu^{2+} ions were intercalated into the interlayer spacing of the pristine NaB during each ion adsorption operation. However, a fraction of the intercalated Cu^{2+} ions and the original stabilizing Na^+ ions were deintercalated from the interlayer region simultaneously during each ion desorption operation, leading to a gradual structural evolution from pure Na-birnessite to a mixture of poorly crystallized Cu-birnessite, Cu-buserite, and the cycled Na-birnessite.[59,67,68] The phase transformation is also likely to occur in the cases of KB/C and MgB/C electrodes cycled in Cu^{2+}-bearing saline water (Figures 5b and S17b), although the peaks corresponding to the Cu-buserite in the XRD pattern of KB/C after 60 cycles are difficult to identify (Figure S17b). Nevertheless, considering that Cu-LMOs could be easily obtained by ion exchange of Na-LMO minerals with Cu^{2+} ions[55,56] and that phase transformations between birnessite and buserite were of common occurrence,[36,37,41,49,52] we believe that both Cu-buserite and Cu-birnessite are formed during the cycling operation of Na-LMO in Cu^{2+}-bearing saline water. Furthermore, a decreased d_{001} spacing of 9.40 Å in MgB after cycling in a 100 mg L^{-1} of Cu^{2+} solution was also observed. This is attributed to the smaller radius of hydrated Cu^{2+} ions than that of hydrated Mg^{2+} ions (see Table S3),[37] further confirming the formation of Cu-buserite.

Generally, it is suggested that Cu^{2+} ions are likely to be reduced to copper metal (Cu^0) by electrodeposition at a cell voltage higher than 0.8 V.[69] However, our XPS data of the MgB/C electrodes after 60 cycles in a 100 mg L^{-1} Cu^{2+} saline at 0.8−1.2 V (Figures 5c and S18a) indicate that a small fraction of Cu^{2+} appears to be reduced into Cu^0 (see the small peak of 919 eV in Cu LMM region in Figure 5c) at a cell voltage of 0.8 V, while most of the Cu species are present as Cu^{2+} (see the strong Cu^{2+} satellite area in the Cu 2p XPS region in Figure 5c). In addition, no electrodeposition occurs for both the cathodes and the anodes when the cell voltages are beyond 0.8 V (Figure S18). This phenomenon is contrary to the observation that steady electrodeposition of Cu^{2+} often occurs at a voltage of 2.0 V.[70] We speculate that this paradox is likely caused by the overlong analysis of the sample, as some Cu(II) compounds may be reduced by prolonged XPS analysis.[71]

Cu^{2+} ion has also demonstrated a higher stabilizing power toward LMO minerals than other ions (i.e., Na^+, K^+, Ca^{2+}, and Mg^{2+}) due to its higher affinity to LMO minerals. Adsorption of Cu^{2+} could decrease the surface energy of LMO minerals and thereby improve their thermodynamic stability.[59] This phenomenon explains why there were no peaks assignable to other manganese oxide minerals beyond LMOs in the XRD patterns of LMO/C after 60 cycles (Figures 5b and S17b). Spectroscopic experiments have shown that Cu^{2+} binds to LMO minerals by inner-sphere complexation on the surface site or structurally incorporates into the MnO_6 layers by occupying the vacancy sites.[72] Therefore, the mechanism of Cu trapping by the LMO/C electrodes from solution is likely to be involved in the intercalation reaction, surface complexation, and structural incorporation (Figure 5d). Furthermore, the atomic ratio of the surface elements at MgB/C electrodes after

https://doi.org/10.1021/acsami.2c13086
ACS Appl. Mater. Interfaces 2022, 14, 46646−46656

60 cycles in a 100 mg L^{-1} Cu^{2+} saline at 1.2 V is 59.51:20.87:11.36:7.3:0.96 for C/O/F/Mn/Cu according to the XPS survey data (Figure S18a). The concentration of Cu^{2+} in the HCDI cell was measured by ICP-OES to be 2.04 mg L^{-1} and the mass of PVDF was predefined to be 6.25 mg (0.05/8 g). Assuming that all surface Cu is surface-complexed Cu^{2+}, the contributions from surface complexation and intercalation to Cu^{2+} uptake on the MgB/C electrodes in the HCDI platform can be calculated to be 26.7 and 73.3%, respectively (Figure S19).

CONCLUSIONS

Mg-buserite was prepared via ion exchange of Na-birnessite and exhibited a larger interlayer spacing compared to Na- and K-birnessite. The Mg-buserite/C was employed as electrodes in an HCDI system and demonstrated superior deionization performance in electrosorption of both alkali and alkaline earth metal ions compared to the Na- and K-birnessite/C electrodes. Besides, Mg-buserite/C showed the highest Cu^{2+} ion adsorption capacity (IAC) of 89.3 mg Cu^{2+} per gram electrode materials at a cell voltage of 1.2 V in 500 mg L^{-1} $CuCl_2$ solution, with an IAC retention as high as 96.3% after 60 charge/discharge cycles. In addition, data of deionization cycling in equimolar ternary saline imply that Mg-buserite/C exhibited a preference toward Cu^{2+} over other monovalent (i.e., Na^+ and K^+) and divalent ions (i.e., Ca^{2+} and Mg^{2+}), reaching average selectivity values of 4.7, 7.7, and 8.1 for Cu^{2+} over Na^+, Ca^{2+}, and Mg^{2+}, respectively. Furthermore, X-ray diffraction and spectroscopic measurements reveal that no Cu^{2+} electrodeposition occurs during the HCDI operation and that both electrosorption (via intercalation) and surface complexation contribute to the uptake of Cu^{2+} on the Mg-buserite/C electrodes. Therefore, HCDI using Mg-buserite/C as electrodes is promising for preferential Cu^{2+} removal when competing with co-occurring alkali and alkaline metal ions, which can have applications in desalination or copper recovery from industrial wastewater. In conclusion, the strategy of tailoring the interlayer spacing of layered manganese oxide (LMO) materials for enhanced and selective removal of specific heavy metal ions can be further extended to other redox-active materials applied for CDI platforms.

ASSOCIATED CONTENT

Supporting Information

The Supporting Information is available free of charge at https://pubs.acs.org/doi/10.1021/acsami.2c13086.

Experimental details; scheme of HCDI setup; XPS spectra, FTIR and XRF spectra, SEM images, N_2 adsorption−desorption isotherms, and pore size distribution of the LMOs; CV curves, GCD curves, IR drop plots, specific capacitances plots, and Nyquist plots of EIS of the LMO/C electrodes; desalination performance curves; Kim-Yoon plots, ion adsorption capacity plots; pH and conductivity plots; contour plots; XRD patterns of the LMO/C electrodes before and after cycling in 100 mg L^{-1} Cu^{2+} saline; comparison of SACs, IACs; XPS spectra of the MgB/C electrodes, and supplementary references (PDF)

AUTHOR INFORMATION

Corresponding Author

Feihu Li − *Collaborative Innovation Center of Atmospheric Environment and Equipment Technology, Jiangsu Key Laboratory of Atmospheric Environment Monitoring and Pollution Control, School of Environmental Science and Engineering, Nanjing University of Information Science and Technology, Nanjing 210044, China;* orcid.org/0000-0002-2969-8276; Email: fhli@nuist.edu.cn

Authors

Yang Bao − *Collaborative Innovation Center of Atmospheric Environment and Equipment Technology, Jiangsu Key Laboratory of Atmospheric Environment Monitoring and Pollution Control, School of Environmental Science and Engineering, Nanjing University of Information Science and Technology, Nanjing 210044, China;* orcid.org/0000-0002-5588-2042

Jie Jin − *Collaborative Innovation Center of Atmospheric Environment and Equipment Technology, Jiangsu Key Laboratory of Atmospheric Environment Monitoring and Pollution Control, School of Environmental Science and Engineering, Nanjing University of Information Science and Technology, Nanjing 210044, China*

Mengyu Ma − *Collaborative Innovation Center of Atmospheric Environment and Equipment Technology, Jiangsu Key Laboratory of Atmospheric Environment Monitoring and Pollution Control, School of Environmental Science and Engineering, Nanjing University of Information Science and Technology, Nanjing 210044, China*

Man Li − *Collaborative Innovation Center of Atmospheric Environment and Equipment Technology, Jiangsu Key Laboratory of Atmospheric Environment Monitoring and Pollution Control, School of Environmental Science and Engineering, Nanjing University of Information Science and Technology, Nanjing 210044, China*

Complete contact information is available at: https://pubs.acs.org/10.1021/acsami.2c13086

Author Contributions

†Y.B. and J.J. contributed equally.

Notes

An earlier version of this manuscript has been deposited on the preprint server ChemRixv (https://doi.org/10.26434/chemrxiv-2021-dvtjw).

The authors declare no competing financial interest.

ACKNOWLEDGMENTS

The work was partially supported by NSFC (51002080), the Top-notch Academic Programs Project of Jiangsu Higher Education Institutions (PPZY2015C222), and the Priority Academic Program Development (PAPD) of Jiangsu Higher Education Institutions.

REFERENCES

(1) Shannon, M. A.; Bohn, P. W.; Elimelech, M.; Georgiadis, J. G.; Marinas, B. J.; Mayes, A. M. Science and technology for water purification in the coming decades. *Nature* **2008**, *452* (7185), 301−310.

(2) Su, X.; Kushima, A.; Halliday, C.; Zhou, J.; Li, J.; Hatton, T. A. Electrochemically-mediated selective capture of heavy metal chromium and arsenic oxyanions from water. *Nat. Commun.* **2018**, *9*, 4701.

(3) Huang, C. C.; Su, Y. J. Removal of copper ions from wastewater by adsorption/electrosorption on modified activated carbon cloths. *J. Hazard. Mater.* **2010**, *175* (1−3), 477−483.
(4) Yang, X.; Liu, L. H.; Tan, W. F.; Qiu, G. H.; Liu, F. High-performance Cu2+ adsorption of birnessite using electrochemically controlled redox reactions. *J. Hazard. Mater.* **2018**, *354*, 107−115.
(5) Jin, W.; Hu, M. Q. High-Performance Capacitive Deionization of Copper Ions at Nanoporous ZnS-Decorated Carbon Felt. *J. Electrochem. Soc.* **2019**, *166* (2), E29−E34.
(6) You, S. M.; Tasi, C. K.; Millet, P.; Doong, R. A. Electrochemically capacitive deionization of copper (II) using 3D hierarchically reduced graphene oxide architectures. *Sep. Purif. Technol.* **2020**, *251*, 117368.
(7) Al-Saydeh, S. A.; El-Naas, M. H.; Zaidi, S. J. Copper removal from industrial wastewater: A comprehensive review. *J. Ind. Eng. Chem.* **2017**, *56*, 35−44.
(8) Zhao, R.; Biesheuvel, P. M.; van der Wal, A. Energy consumption and constant current operation in membrane capacitive deionization. *Energy Environ. Sci.* **2012**, *5* (11), 9520−9527.
(9) Suss, M. E.; Porada, S.; Sun, X.; Biesheuvel, P. M.; Yoon, J.; Presser, V. Water desalination via capacitive deionization: what is it and what can we expect from it? *Energy Environ. Sci.* **2015**, *8* (8), 2296−2319.
(10) Gupta, S. S.; Islam, M. R.; Pradeep, T. Chapter 7 - Capacitive Deionization (CDI): An Alternative Cost-Efficient Desalination Technique. In *Advances in Water Purification Techniques*; Ahuja, S., Ed.; Elsevier: 2019; pp 165−202.
(11) Oren, Y. Capacitive deionization (CDI) for desalination and water treatment - past, present and future (a review). *Desalination* **2008**, *228* (1−3), 10−29.
(12) AlMarzooqi, F. A.; Al Ghaferi, A. A.; Saadat, I.; Hilal, N. Application of Capacitive Deionisation in water desalination: A review. *Desalination* **2014**, *342*, 3−15.
(13) Maarof, H. I.; Daud, W. M. A. W.; Aroua, M. K. Recent trends in removal and recovery of heavy metals from wastewater by electrochemical technologies. *Rev. Chem. Eng.* **2017**, *33* (4), 359−386.
(14) Chen, R.; Sheehan, T.; Ng, J. L.; Brucks, M.; Su, X. Capacitive deionization and electrosorption for heavy metal removal. *Environ. Sci.- Water Res. Technol.* **2020**, *6* (2), 258−282.
(15) Zhang, X. D.; Zuo, K. C.; Zhang, X. R.; Zhang, C. Y.; Liang, P. Selective ion separation by capacitive deionization (CDI) based technologies: a state-of-the-art review. *Environ. Sci.- Water Res. Technol.* **2020**, *6* (2), 243−257.
(16) Gamaethiralalage, J. G.; Singh, K.; Sahin, S.; Yoon, J.; Elimelech, M.; Suss, M. E.; Liang, P.; Biesheuvel, P. M.; Zornitta, R. L.; de Smet, L. C. P. M. Recent advances in ion selectivity with capacitive deionization. *Energy Environ. Sci.* **2021**, *14* (3), 1095−1120.
(17) Uwayid, R.; Guyes, E. N.; Shocron, A. N.; Gilron, J.; Elimelech, M.; Suss, M. E. Perfect divalent cation selectivity with capacitive deionization. *Water Res.* **2022**, *210*, 117959.
(18) Guyes, E. N.; Shocron, A. N.; Chen, Y. K.; Diesendruck, C. E.; Suss, M. E. Long-lasting, monovalent-selective capacitive deionization electrodes. *npj Clean Water* **2021**, *4* (1), 22.
(19) Chen, T.-H.; Cuong, D. V.; Jang, Y.; Khu, N.-Z.; Chung, E.; Hou, C.-H. Cation selectivity of activated carbon and nickel hexacyanoferrate electrode materials in capacitive deionization: A comparison study. *Chemosphere* **2022**, *307*, 135613.
(20) Srimuk, P.; Su, X.; Yoon, J.; Aurbach, D.; Presser, V. Charge-transfer materials for electrochemical water desalination, ion separation and the recovery of elements. *Nat. Rev. Mater.* **2020**, *5* (7), 517−538.
(21) Kim, K.; Candeago, R.; Rim, G.; Raymond, D.; Park, A. H. A.; Su, X. Electrochemical approaches for selective recovery of critical elements in hydrometallurgical processes of complex feedstocks. *iScience* **2021**, *24* (5), 102374.
(22) Huang, Z. H.; Yang, Z. Y.; Kang, F. Y.; Inagaki, M. Carbon electrodes for capacitive deionization. *J. Mater. Chem. A* **2017**, *5* (2), 470−496.
(23) Liu, P. Y.; Yan, T. T.; Shi, L. Y.; Park, H. S.; Chen, X. C.; Zhao, Z. G.; Zhang, D. S. Graphene-based materials for capacitive deionization. *J. Mater. Chem. A* **2017**, *5* (27), 13907−13943.
(24) Huang, C. C.; He, J. C. Electrosorptive removal of copper ions from wastewater by using ordered mesoporous carbon electrodes. *Chem. Eng. J.* **2013**, *221*, 469−475.
(25) Li, J.; Wang, X. X.; Wang, H. Q.; Wang, S. H.; Hayat, T.; Alsaedi, A.; Wang, X. K. Functionalization of biomass carbonaceous aerogels and their application as electrode materials for electro-enhanced recovery of metal ions. *Environ. Sci.- Nano* **2017**, *4* (5), 1114−1123.
(26) Wang, H.; Yan, T. T.; Shen, J. J.; Zhang, J. P.; Shi, L. Y.; Zhang, D. S. Efficient removal of metal ions by capacitive deionization with straw waste derived graphitic porous carbon nanosheets. *Environ. Sci.-Nano* **2020**, *7* (1), 317−326.
(27) Moronshing, M.; Subramaniam, C. Scalable Approach to Highly Efficient and Rapid Capacitive Deionization with CNT-Thread As Electrodes. *ACS Appl. Mater. Interfaces* **2017**, *9* (46), 39907−39915.
(28) Hu, C. Z.; Liu, F. Y.; Lan, H. C.; Liu, H. J.; Qu, J. H. Preparation of a manganese dioxide/carbon fiber electrode for electrosorptive removal of copper ions from water. *J. Colloid Interface Sci.* **2015**, *446*, 359−365.
(29) Liu, Y. H.; Hsi, H. C.; Li, K. C.; Hou, C. H. Electrodeposited Manganese Dioxide/Activated Carbon Composite As a High-Performance Electrode Material for Capacitive Deionization. *ACS Sustain. Chem. Eng.* **2016**, *4* (9), 4762−4770.
(30) Zhao, C. J.; Wang, X. L.; Zhang, S. B.; Sun, N.; Zhou, H. J.; Wang, G. Z.; Zhang, Y. X.; Zhang, H. M.; Zhao, H. J. Porous carbon nanosheets functionalized with Fe3O4 nanoparticles for capacitive removal of heavy metal ions from water. *Environ. Sci.- Water Res. Technol.* **2020**, *6* (2), 331−340.
(31) Mao, M. L.; Yan, T. T.; Chen, G. R.; Zhang, J. P.; Shi, L. Y.; Zhang, D. S. Selective Capacitive Removal of Pb2+ from Wastewater over Redox-Active Electrodes. *Environ. Sci. Technol.* **2021**, *55* (1), 730−737.
(32) Wu, S. J.; Yan, P. J.; Yang, W.; Zhou, J.; Wang, H.; Che, L.; Zhu, P. F. ZnCl2 enabled synthesis of activated carbons from ion-exchange resin for efficient removal of Cu2+ ions from water via capacitive deionization. *Chemosphere* **2021**, *264*, 128557.
(33) Bautista-Patacsil, L.; Lazarte, J. P. L.; Dipasupil, R. C.; Pasco, G. Y.; Eusebio, R. C.; Orbecido, A.; Doong, R. Deionization utilizing reduced graphene oxide-titanium dioxide nanotubes composite for the removal of Pb2+ and Cu2+. *J. Environ. Chem. Eng.* **2020**, *8* (3), 103063.
(34) Lee, J.; Kim, S.; Kim, C.; Yoon, J. Hybrid capacitive deionization to enhance the desalination performance of capacitive techniques. *Energy Environ. Sci.* **2014**, *7* (11), 3683−3689.
(35) Liu, L. H.; Qiu, G. H.; Suib, S. L.; Liu, F.; Zheng, L. R.; Tan, W. F.; Qin, L. H. Enhancement of Zn2+ and Ni2+ removal performance using a deionization pseudocapacitor with nanostructured birnessite and its carbon nanotube composite electrodes. *Chem. Eng. J.* **2017**, *328*, 464−473.
(36) Byles, B. W.; Cullen, D. A.; More, K. L.; Pomerantseva, E. Tunnel structured manganese oxide nanowires as redox active electrodes for hybrid capacitive deionization. *Nano Energy* **2018**, *44*, 476−488.
(37) Byles, B. W.; Hayes-Oberst, B.; Pomerantseva, E. Ion Removal Performance, Structural/Compositional Dynamics, and Electrochemical Stability of Layered Manganese Oxide Electrodes in Hybrid Capacitive Deionization. *ACS Appl. Mater. Interfaces* **2018**, *10* (38), 32313−32322.
(38) Leong, Z. Y.; Yang, H. Y. A Study of MnO2 with Different Crystalline Forms for Pseudocapacitive Desalination. *ACS Appl. Mater. Interfaces* **2019**, *11* (14), 13176−13184.
(39) Jin, J.; Li, M.; Tang, M. T.; Li, Y.; Liu, Y. Y.; Cao, H.; Li, F. H. Phase- and Crystallinity-Tailorable MnO2 as an Electrode for Highly Efficient Hybrid Capacitive Deionization (HCDI). *ACS Sustain. Chem. Eng.* **2020**, *8* (30), 11424−11434.

https://doi.org/10.1021/acsami.2c13086
ACS Appl. Mater. Interfaces 2022, 14, 46646−46656

(40) Zhao, Y. B.; Liang, B. L.; Zong, M. Z.; Duan, M.; Li, K. X.; Lv, C. C. Different crystallographic sodium manganese oxides for capacitive deionization: performance comparison and the associated mechanism. *Environ. Sci.- Nano* **2019**, *6* (10), 3091−3101.
(41) Post, J. E. Manganese oxide minerals: Crystal structures and economic and environmental significance. *Proc. Nat. Acad. Sci. U.S.A.* **1999**, *96* (7), 3447−3454.
(42) Liu, L. H.; Tan, W. F.; Suib, S. L.; Qiu, G. H.; Zheng, L. R.; Huang, Q. Y.; Liu, C. S. Effective Zinc Adsorption Driven by Electrochemical Redox Reactions of Birnessite Nanosheets Generated by Solar Photochemistry. *ACS Sustain. Chem. Eng.* **2018**, *6* (11), 13907−13914.
(43) Chen, L.; Shi, G. S.; Shen, J.; Peng, B. Q.; Zhang, B. W.; Wang, Y. Z.; Bian, F. G.; Wang, J. J.; Li, D. Y.; Qian, Z.; et al. Ion sieving in graphene oxide membranes via cationic control of interlayer spacing. *Nature* **2017**, *550* (7676), 415−418.
(44) Liu, X. M.; Zhang, L.; Gao, X. R.; Guan, C.; Hu, Y. T.; Wang, J. Enlarged Interlayer Spacing in Cobalt-Manganese Layered Double Hydroxide Guiding Transformation to Layered Structure for High Supercapacitance. *ACS Appl. Mater. Interfaces* **2019**, *11* (26), 23236−23243.
(45) Sarkar, D.; Das, D.; Das, S.; Kumar, A.; Patil, S.; Nanda, K. K.; Sarma, D. D.; Shukla, A. Expanding Interlayer Spacing in MoS2 for Realizing an Advanced Supercapacitor. *ACS Energy Lett.* **2019**, *4* (7), 1602−1609.
(46) Wang, S. Y.; Wang, G.; Che, X. P.; Wang, S. F.; Li, C. X.; Li, D. Z.; Zhang, Y. Q.; Dong, Q.; Qiu, J. S. Enhancing the capacitive deionization performance of NaMnO2 by interface engineering and redox-reaction. *Environ. Sci.- Nano* **2019**, *6* (8), 2379−2388.
(47) Feng, Q.; Sun, E. H.; Yanagisawa, K.; Yamasaki, N. Synthesis of birnessite-type sodium manganese oxides by solution reaction and hydrothermal methods. *J. Ceram. Soc. Jpn.* **1997**, *105* (7), 564−568.
(48) Kim, T.; Gorski, C. A.; Logan, B. E. Ammonium Removal from Domestic Wastewater Using Selective Battery Electrodes. *Environ. Sci. Technol. Lett.* **2018**, *5* (9), 578−583.
(49) Feng, Q.; Kanoh, H.; Ooi, K. Manganese oxide porous crystals. *J. Mater. Chem.* **1999**, *9* (2), 319−333.
(50) Biesinger, M. C.; Payne, B. P.; Grosvenor, A. P.; Lau, L. W. M.; Gerson, A. R.; Smart, R. S. Resolving surface chemical states in XPS analysis of first row transition metals, oxides and hydroxides: Cr, Mn, Fe, Co and Ni. *Appl. Surf. Sci.* **2011**, *257* (7), 2717−2730.
(51) Wachs, I. E. Infrared-Spectroscopy of Supported Metal-Oxide Catalysts. *Colloids Surf., A* **1995**, *105* (1), 143−149.
(52) Wei, W. F.; Cui, X. W.; Chen, W. X.; Ivey, D. G. Manganese oxide-based materials as electrochemical supercapacitor electrodes. *Chem. Soc. Rev.* **2011**, *40* (3), 1697−1721.
(53) Lukatskaya, M. R.; Dunn, B.; Gogotsi, Y. Multidimensional materials and device architectures for future hybrid energy storage. *Nat. Commun.* **2016**, *7*, 12647.
(54) Brousse, T.; Belanger, D.; Long, J. W. To Be or Not To Be Pseudocapacitive? *J. Electrochem. Soc.* **2015**, *162* (5), A5185−A5189.
(55) Lei, Z. B.; Shi, F. H.; Lu, L. Incorporation of MnO2-Coated Carbon Nanotubes between Graphene Sheets as Supercapacitor Electrode. *ACS Appl. Mater. Interfaces* **2012**, *4* (2), 1058−1064.
(56) Mao, M. L.; Yan, T. T.; Shen, J. J.; Zhang, J. P.; Zhang, D. S. Capacitive Removal of Heavy Metal Ions from Wastewater via an Electro-Adsorption and Electro-Reaction Coupling Process. *Environ. Sci. Technol.* **2021**, *55* (5), 3333−3340.
(57) McNair, R.; Szekely, G.; Dryfe, R. A. W. Ion-Exchange Materials for Membrane Capacitive Deionization. *Acs ES&T Water* **2021**, *1* (2), 217−239.
(58) Yin, J. F.; Takeuchi, E. S.; Takeuchi, K. J.; Marschilok, A. C. Synthetic control of manganese birnessite: Impact of crystallite size on Li, Na, and Mg based electrochemistry. *Inorg. Chim. Acta* **2016**, *453*, 230−237.
(59) Yang, P.; Post, J. E.; Wang, Q.; Xu, W. Q.; Geiss, R.; McCurdy, P. R.; Zhu, M. Q. Metal Adsorption Controls Stability of Layered Manganese Oxides. *Environ. Sci. Technol.* **2019**, *53* (13), 7453−7462.
(60) Choi, S.; Chang, B.; Kim, S.; Lee, J.; Yoon, J.; Choi, J. W. Battery Electrode Materials with Omnivalent Cation Storage for Fast and Charge-Efficient Ion Removal of Asymmetric Capacitive Deionization. *Adv. Funct. Mater.* **2018**, *28* (35), 1802665.
(61) Mao, M. L.; Yan, T. T.; Shen, J. J.; Zhang, J. P.; Zhang, D. S. Selective Capacitive Removal of Heavy Metal Ions from Wastewater over Lewis Base Sites of S-Doped Fe-N-C Cathodes via an Electro-Adsorption Process. *Environ. Sci. Technol.* **2021**, *55* (11), 7665−7673.
(62) He, D.; Wong, C. E.; Tang, W. W.; Kovalsky, P.; Waite, T. D. Faradaic Reactions in Water Desalination by Batch-Mode Capacitive Deionization. *Environ. Sci. Technol. Lett.* **2016**, *3* (5), 222−226.
(63) Gao, X.; Omosebi, A.; Landon, J.; Liu, K. L. Surface charge enhanced carbon electrodes for stable and efficient capacitive deionization using inverted adsorption-desorption behavior. *Energy Environ. Sci.* **2015**, *8* (3), 897−909.
(64) Singh, K.; Li, G.; Lee, J.; Zuilhof, H.; Mehdi, B. L.; Zornitta, R. L.; de Smet, L. C. P. M. Divalent Ion Selectivity in Capacitive Deionization with Vanadium Hexacyanoferrate: Experiments and Quantum-Chemical Computations. *Adv. Funct. Mater.* **2021**, *31* (41), 2105203.
(65) Leong, Z. Y.; Zhang, J. T.; Vafakhah, S.; Ding, M.; Guo, L.; Yang, H. Y. Electrochemically activated layered manganese oxide for selective removal of calcium and magnesium ions in hybrid capacitive deionization. *Desalination* **2021**, *520*, 115374.
(66) Li, D. Z.; Wang, S. Y.; Wang, G.; Li, C. X.; Che, X. P.; Wang, S. F.; Zhang, Y. Q.; Qiu, J. S. Facile Fabrication of NiCoAl-Layered Metal Oxide/Graphene Nanosheets for Efficient Capacitive Deionization Defluorination. *ACS Appl. Mater. Interfaces* **2019**, *11* (34), 31200−31209.
(67) Feng, X. H.; Zhao, H. Y.; Liu, F.; Cui, H. J.; Tan, W. F.; Li, W. Transformation from Phyllomanganates to Todorokite under Various Conditions: A Review of Implication for Formation Pathway of Natural Todorokite. *ACS Symp. Ser.* **2015**, *1197*, 107−134.
(68) Li, Y. R.; Marschilok, A. C.; Takeuchi, E. S.; Takeuchi, K. J. Synthesis of Copper Birnessite, CuxMnOy·nH2O with Crystallite Size Control: Impact of Crystallite Size on Electrochemistry. *J. Electrochem. Soc.* **2016**, *163* (2), A281−A285.
(69) Huang, S. Y.; Fan, C. S.; Hou, C. H. Electro-enhanced removal of copper ions from aqueous solutions by capacitive deionization. *J. Hazard. Mater.* **2014**, *278*, 8−15.
(70) Chen, L.; Zhang, G.; Shan, W. Y.; Liu, R.; Liu, H. J. Potential Oscillated Electrochemical Metal Recovery System with Improved Conversion Kinetics and High Levelized Quality. *Environ. Sci. Technol.* **2021**, *55* (22), 15380−15389.
(71) *Avantage Software, XPS Knowledge Database*, version 5.979; Thermo Fisher Scientific Inc.: Waltham, MA, 2017. https://www.thermofisher.com/order/catalog/product/IQLAADGACKFAKRMAVI.
(72) Sherman, D. M.; Peacock, C. L. Surface complexation of Cu on birnessite (δ-MnO2): Controls on Cu in the deep ocean. *Geochim. Cosmochim. Acta* **2010**, *74* (23), 6721−6730.

https://doi.org/10.1021/acsami.2c13086
ACS Appl. Mater. Interfaces 2022, 14, 46646−46656